Quantitative laboratory observations of internal wave reflection on ascending slopes

Louis Gostiaux and Thierry Dauxois
Laboratoire de Physique, UMR-CNRS 5672, ENS Lyon, 46 Allée d'Italie, 69364 Lyon Cédex 07, France

Henri Didelle, Joel Sommeria, and Samuel Viboud
Laboratoire des Écoulements Geophysiques et Industriels (LEGI), UMR 5519 CNRS-UJF-INPG, 21 rue des Martyrs, 38000 Grenoble, France

Internal waves propagate obliquely through a stratified fluid with an angle that is fixed with respect to gravity. Upon reflection on a sloping bed, striking phenomena are expected to occur close to the slope. We present here laboratory observations at moderately large Reynolds number. A particle image velocimetry technique is used to provide time-resolved velocity fields in large volumes. Generation of the second and third harmonic frequencies is clearly demonstrated in the impact zone. The mechanism for nonlinear wavelength selection is also discussed. Evanescent waves with frequency larger than the Brunt-Väisälä frequency are detected and experimental results agree very well with theoretical predictions. The amplitude of the different harmonics after reflection is also obtained. © *2006 American Institute of Physics*. [DOI: 10.1063/1.2197528]

I. INTRODUCTION

The oblique propagation of internal waves follows from the dispersion relation that monochromatic perturbations of frequency ω have to satisfy

$$\omega = \pm N \sin \theta, \tag{1}$$

where N is the Brunt-Väisälä frequency

$$N = \sqrt{-\frac{g}{\rho_0}\frac{\partial \rho}{\partial z}}, \tag{2}$$

g being the gravity, $\rho(z)$ the ambient density profile, and ρ_0 a reference density. This dispersion relation shows that for a fixed frequency, the direction in which energy propagates with respect to the horizontal, θ, is fixed. Moreover, Eq. (1) determines that phase and energy propagate in perpendicular directions. For setup with Brunt-Väisälä frequency N independent of z, observations of internal waves have invariably showed[2,14] this transverse and oblique propagation.

The above dispersion relation is obtained, away from any turbulent portions of the domain, by substituting a plane wave $A \exp[ik(x \sin \theta + z \cos \theta)]$ of wave umber k and amplitude A in the wave equation governing the horizontal velocity u,

$$u_{ttxx} + u_{ttzz} = -N^2 u_{xx}, \tag{3}$$

where subscripts denote partial derivative, x and z refer to Cartesian coordinates, and t denotes time. The vertical velocity w, the perturbation pressure p, the stream function ψ, and the perturbation density satisfy the same hyperbolic equation (3).

The presence of a solid horizontal bottom, a free surface, or an oblique slope results in a reflected wave with the same intrinsic wave frequency as the incident one. *Linear* internal wave reflection on a sloping bottom has been treated analytically by different authors.[4,17,22] The striking consequence of the geometric focusing of linear internal waves has also been reported.[10–12] Under appropriate conditions, it leads to internal wave attractors in confined stably stratified fluids. For *critically* incident waves for which the slope and energy propagation angles coincide, the linear inviscid analysis becomes singular and an infinite amplitude of the reflected wave was predicted.[17]

Experiments on internal wave reflection were first performed by Cacchione and Wunsch[1] using conductivity probe measurements. A tidal-like excitation was generated in a 5-m-long tank by a horizontally oscillating paddle; the incident and reflected waves from a 15° slope were separated using periodogram estimates to compute wave amplitude and wave number. Although these pioneering results were of poor quality (compared to what is possible nowadays), their shadowgraph experiments showed, nevertheless, striking microstructures along the slope, reminiscent of an array of vortices along the slope's boundary layer. Thorpe and Haines[23] measured dye band displacements on a 20° slope providing qualitative agreement with linear theory and also noticed three-dimensional boundary layer structures. Subsequently, Ivey and Nokes[6] estimated the mixing efficiency above a 30° slope submitted to modal excitation and visualized with the rainbow Schlieren technique: the weakening of the background stratification was measured and the corresponding change in potential energy compared to the mechanical work provided by the wave maker. The internal wave reflection mechanism has also been studied in close connection with its importance for the creation of nepholoid layers by McPhee and Kunze.[13] More recently, Dauxois, Didier, and Falcon[2] performed Schlieren experiments on critical reflection, focusing on the boundary layer upwelling events and providing good qualitative agreement with the previous weakly nonlinear study.[3] Finally, using synthetic Schlieren measurements, Peacock and Tabaei[16] showed the second harmonic genera-

tion. To our knowledge, no local quantitative amplitude measurements of internal wave reflection have been performed so far.

Recently, the *weakly nonlinear* theoretical issue has been put forward. It has been shown by Dauxois and Young[3] that the singularity can be healed using matched asymptotic expansion. Their analysis describes the buildup of the reflected wave along the slope for a incident plane wave. Always from the theoretical point of view, the reflection of internal waves was revisited by Tabaei, Akylas, and Lamb[20] for the case of a narrow incident beam but for noncritical angles. In this case, they have predicted the generation of harmonics in the steady regime; this result has not been addressed experimentally yet. Besides, fully nonlinear numerical simulations have also been performed to examine the behavior of large-amplitude internal gravity waves impinging on a slope.[8,9,18,19,24]

Here we present the results of laboratory experiments in which a beam of internal waves is reflected on an oblique slope. Experiments were carried out in the 13-m-diam Coriolis platform, in Grenoble, filled with salted water. The large scale of the facility allows us to strongly reduce the viscous dissipation along wave propagation and, moreover, quantitative results are obtained thanks to high-resolution particle image velocimetry (PIV) measurements.

The paper is organized as follows. In Sec. II, we present the experimental setup and discuss all control parameters. In Sec. III, we show the experimental results. We explain in Sec. III A the spectral analysis used to distinguish the different harmonics. In Sec. III B, we discuss the mechanism of wavelength selection. Section III C is devoted to the evanescent waves, while Sec. III D discusses amplitude measurements. Section IV concludes and gives some perspectives.

II. EXPERIMENTS

A. Experimental setup

We developed an original internal wave exciter inspired by Ivey *et al.*[7] in order to produce a two-and-a-half wavelengths beam. A PVC sheet was compressed on both sides by seven squared arms (Fig. 1) fixed on a long central axis via eccentric wheels. The axis was set in rotation by a stepping motor, generating a longitudinal oscillation motion of 8 cm amplitude along the 60 cm width of the paddle. The frequency of excitation, proportional to the angular speed of the motor, could be precisely monitored in order to vary the angle of propagation of internal waves. The wavelength was also varied from 11.3 to 12.6 cm. The paddle itself was inclined at an angle $\Phi = 13°$ with the horizontal to increase excitation efficiency. If the main part of the energy is indeed transmitted to a beam of internal wave of frequency ω, higher harmonics $n\omega$ are also excited by the oscillating paddle. Nevertheless, as their frequencies are higher, their propagation angles are also larger. Taking advantage of this fact, a screen has been appropriately located above the bottom-end of the glass plate so that all harmonics are reflected to the left, and do not perturb the region of interest.
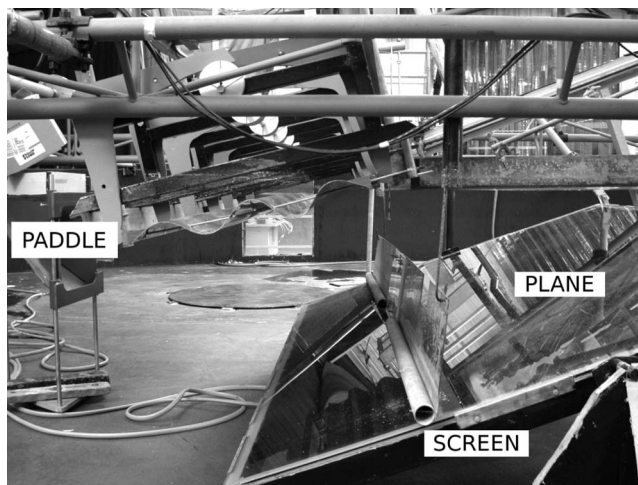

FIG. 1. Picture of the experimental setup. The 3-m-long oscillating paddle generates incident internal waves that are impinging on the inclined glass plane visible on the left. One also clearly sees the screen that avoids the propagation toward the glass plane of harmonics also generated by the paddle. This picture was taken before the 13-m-diam tank has been filled with 1 m of stratified salt water.

The emitted plane wave hits a 2×3 m glass plane (see Fig. 1), back-painted in black to avoid parasite laser beam reflections.

The above experimental setup was put in the 13-m-diam Coriolis tank filled from below with salt water and stratified by computer-controlled volumetric pumps from two 75 m³ tanks, one filled with salt water and the other one with pure water. A fast conductivity probe and a temperature probe were lowered slowly into the tank using a controlled vertical microstepping motor to measure the stratification. The density probe was calibrated using an Anton Paar densitometer accurate to 0.0001 kg/m³ and 0.01 °C. The linearity of the resulting density gradient was of very good accuracy, and only the upper 5 cm and the bottom 10 cm were not linearly stratified. Observations have thus been performed in the intermediate region where the Brunt-Väisälä frequency is a very well defined constant.

The stratification of 2.2% over the 1 m depth of the tank led to a Brunt-Väisälä period $2\pi N^{-1} = 13.6$ s. All experiments we discuss here were performed without rotation of the tank, and thus involve pure internal waves.

We used the PIV facility of the Coriolis Platform to obtain top and side views of the velocity field. The fluid was seeded with 400 microns diameter particle polystyrene beads that were carefully prepared by a process of cooking that decreases slightly the density and successive density separations. One thus obtains a flat distribution of densities matching that of the salt stratification. This process ensures that there are equal number densities of particles at each depth. A surfactant was added to prevent the polystyrene beads from clustering. It has been shown that the relaxation time for particles to attain velocity equilibrium[15] is about 0.02 s, which is much shorter than the characteristic time scale of the flow. As usual, the particles are considered as passive tracers of the fluid motion.

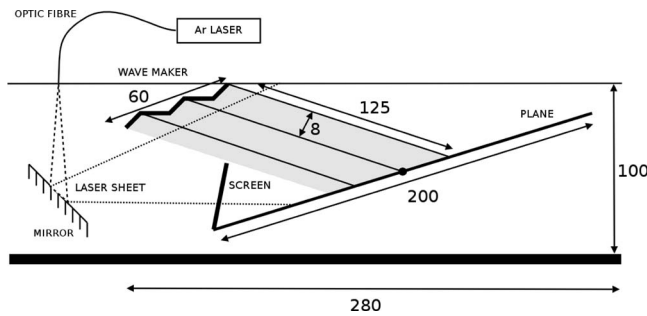With this method, motion is visualized by illuminating

FIG. 2. Sketch of the vertical cross-section of the experimental setup. The sinusoidal thick line on the top left indicates the position of the oscillating paddle, while the gray region defines the incident beam impinging on the sloping glass plane. The optic fiber, indicated by the solid line on the left, shines a laser light that is reflected on the underwater 45 degree mirror, making a thin vertical laser sheet necessary for the PIV measurements. Finally, the dashed line shows the position of the screen that avoids the propagation toward the glass plate of harmonics also generated by the paddle. A slit in the screen allows the laser sheet to pass through. All distances are in centimeters.

TABLE I. Summary of experimental runs with all control parameters. T is the excitation period, θ the angle of energy propagation, α the angle of the slope defined in Fig. 3, and λ the wavelength of the incident beam. u_{max} is the maximum horizontal velocity that has been measured.

Run	1	2	3	4	5
T (s)	60	49	41.5	36	32
θ (deg)	13	16	19	22	25
α (deg)	22	22	22	22	22
λ (cm)	11.3	11.7	12.0	12.2	12.6
u_{max} (cm/s)	0.412	0.566	0.775	1.000	1.225

particles with a laser sheet, which are followed by a digital camera. The laser is intentionally kept out of focus (approximately 1 cm sheet width), enabling tracking of particles despite some cross sheet displacement. Velocity fields within the plane of the laser sheet are obtained by comparing patterns in two subsequent image frames (taken 1 s apart).

The 6 W green argon laser was placed above the free surface, and the light was reflected on a 45 degree mirror placed in the water (see Fig. 2). Thanks to a second underwater 45 degree mirror, the images were acquired by a 1024×1024 pixels CCD camera also located above the free surface. The cross-correlation PIV algorithm designed by Fincham and Delerce[5] was used to convert the images into vector fields (stored in the standard file format NetCDF). This algorithm provides good anti-aliasing and peak-locking rejection procedures. Our resolution went to subpixels distortions, corresponding to submillimetric displacements of the fluid. Typical maximal displacement in an image pair corresponds to 5 pixels, with a measurement precision of 0.2 pixel for an individual field (4% relative precision). This is mostly a random error, so the precision on averaged fields is higher. Finally, the analysis of the NetCDF files was performed with Matlab software.

Typical experimental runs lasted about 20 min. The first 10 periods were considered as an initial transient. Data were thus only recorded throughout the second stage during which the steady regime was attained.

B. Characteristics of the incident wave beam

The set of chosen excitation periods (see Table I and Fig. 3) leads through the dispersion relation (1) to different angles of propagation θ ranging from 13° to 25°. As the slope angle α is set to 22°, these cases allow us to analyze subcritical ($\theta < \alpha$), supercritical ($\theta > \alpha$), or critical ($\theta \simeq \alpha$) reflections. Finally, as the wave maker is slightly tilted (13°) from the horizontal, one has to take into account that the wavelength varied slightly from one run to another, around a typical value of $\lambda_0 = 12$ cm.

Previous experimental studies of internal wave reflection have reported the importance of viscous dissipation[2,16] to explain the observed steady-state solution. Here, by contrast, the large scale of the experiment allowed us to work at a large Reynolds number. By taking the wavelength and the velocity amplitude of the incident internal wave beam, one gets for the Reynolds number Re $\simeq 100$, which suggests that viscous dissipation might be negligible during the propagation toward the slope of the beam itself. This is what can be verified in Fig. 4, where one has used a synchronous detection-like idea. We have filtered the PIV signal at the excitation frequency ω (see Sec. III A for additional details). As the energy is expected to obliquely propagate with an angle θ with respect to the horizontal, the relevant quantities are the velocity fields $v_s(s,\sigma) = u \cos\theta - w \sin\theta$ and $v_\sigma(s,\sigma) = u \sin\theta + w \cos\theta$. Both have been measured and the first one is reproduced with false color in Fig. 4(a). The longitudinal section presented in Fig. 4(b) with a solid line emphasizes that the amplitude of the incident beam is con-
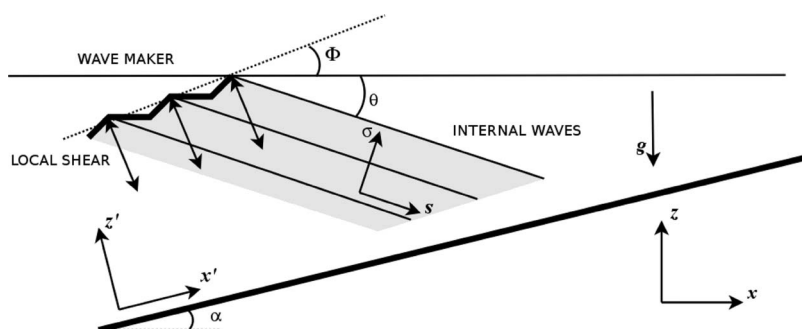

FIG. 3. Definition of variables. Three different coordinate systems will be successively used: the gravity-oriented one (x,z), the slope-oriented one (x',z'), and finally the incident-beam-oriented one (s,σ). The PVC sheet compressed periodically along the dotted line provides a shear flow orthogonal to this line, and thus tilted at a constant angle Φ with the vertical. This flow induces waves propagating at an angle θ with the horizontal, determined by the dispersion relation (1) while α is the slope angle.
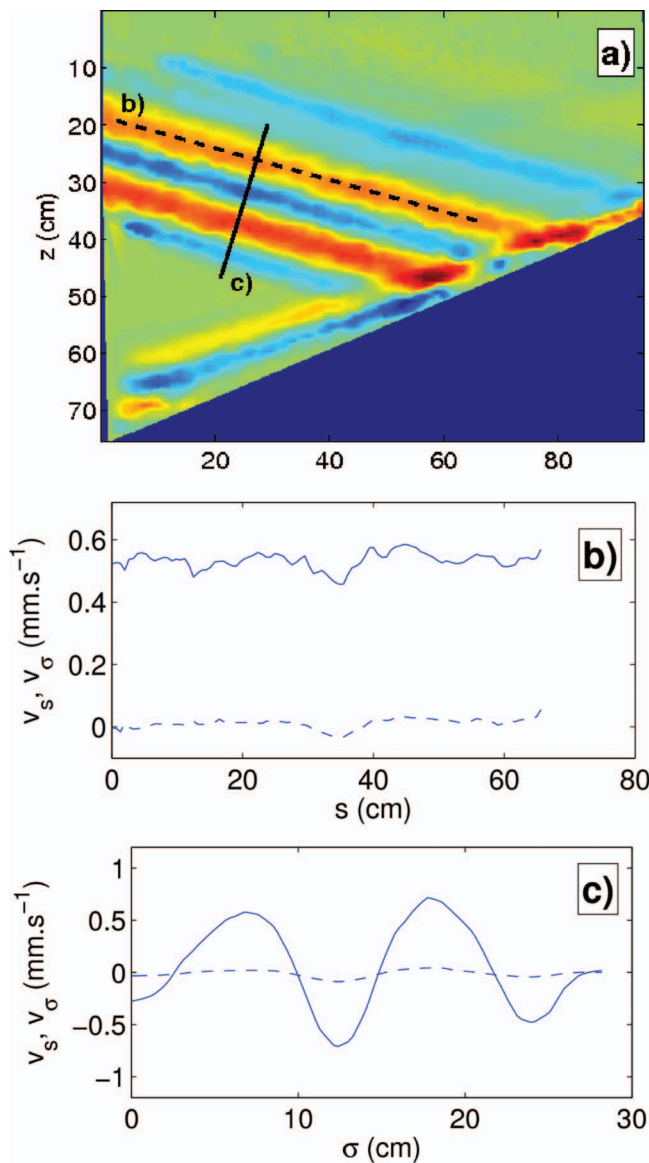
FIG. 4. (Color) False-color pattern of the along-beam $v_s(x,z)$ velocity for $\theta=16°$ and $\alpha=22°$ in a vertical (x,z) section. The shaded triangle corresponds to the region below the glass plate, unperturbed by the internal waves. The maximum velocity in this figure is 0.07 cm s^{-1}. Panels (b) and (c) show the along-beam and cross-beam sections, respectively, indicated by the dashed and solid lines in panel (a). The longitudinal variation v_s is shown in panels (b) and (c) with solid lines, while the dashed lines correspond to the transversal variation v_σ. The longitudinal coordinate s and the transversal one σ are defined in Fig. 3.

stant. The dashed line, which shows the velocity field v_σ along the longitudinal section of Fig. 4(a), is vanishingly small, as expected. This is an important necessary condition to discuss quantitatively the reflection process. Moreover, the picture emphasizes that incident phase planes, which correspond to the same color, are parallel to the direction of the incident group velocity, the latter being indicated by the dashed line. This is a clear demonstration of the orthogonality of the group velocity and the wave vector. Finally, Fig. 4(c) presents v_s along the solid line of Fig. 4(a) and reveals that the width of the beam contains two wavelengths. This is an important point to draw a comparison with theoretical

predictions derived for plane waves.[3] Again, the dashed line attests that the velocity field v_σ is vanishingly small.

III. EXPERIMENTAL RESULTS

A. Spectral analysis

An important characteristic of the reflection of internal waves is the generation of different harmonics, theoretically predicted a long time ago,[3,22] but only very recently experimentally observed.[16] However, the amplitudes of the different harmonics can be very different and, consequently, hardly distinguishable even though their propagation angles are different. A typical example is presented in Fig. 5(a).

This is why we developed a Fourier temporal analysis of the results, with filtering at the fundamental and higher harmonics frequencies. Given the two components of the velocity field provided by the PIV analysis, we compute the filtered velocity fields. For the horizontal one $u(x,y,t)$, one thus defines the different quantities

$$\langle u \rangle_n = \frac{2}{t_1 - t_0} \int_{t_0}^{t_1} u(x,z,t)\cos(n\omega t + \phi)\mathrm{d}t. \qquad (4)$$

In the time interval $[t_0, t_1]$, the amplitude of the nth harmonic $\langle u \rangle_n$ is of course a function of the spatial variables x and z, but also of a constant phase ϕ, chosen with respect to the flat position of the sinusoidal paddle. This procedure is equivalent to band-pass filtering the PIV time series at each point in the domain.

Figures 5(b)–5(d) show that this procedure is an excellent tool to distinguish the different harmonics. Indeed, for this almost critical reflection case (run 4, $\alpha=22°$, $\theta=22\pm1°$), it is clearly apparent in Fig. 5(b) that the reflected beam at frequency ω is absent except a small slightly supercritical along-slope ray. Nevertheless, Figs. 5(c) and 5(d) show the emitted second and third harmonics propagating with steeper angles. The angles of propagation with respect to the horizontal for the second harmonic beam are $\theta_2=48\pm1°$, in agreement with the theoretical value

$$\theta_n = \sin^{-1}(n \sin \theta) \qquad (5)$$

for $n=2$. The third harmonic is evanescent; its characteristics will be discussed in Sec. III C. Both harmonics are generated in the finite domain region, adjacent to the bottom, where the incident beam hits the slope. One should not take into account the few rays located at the left of the arrows [see Figs. 5(c) and 5(d)]: they were generated by the oscillations of the screen. The emitted second harmonic between the two arrows can still be spatially distinguished from these artifacts. It is important to emphasize that the color scales differ by a factor 5 between the first two panels and the last two.

In summary, Fig. 5 exemplified that, even though the second and third harmonics are almost invisible from the instantaneous velocity field, they are very clearly apparent after the filtering procedure. This filtering method is consequently appropriate even when the amplitude is very small. To our knowledge, even if it were previously predicted,[20,22]
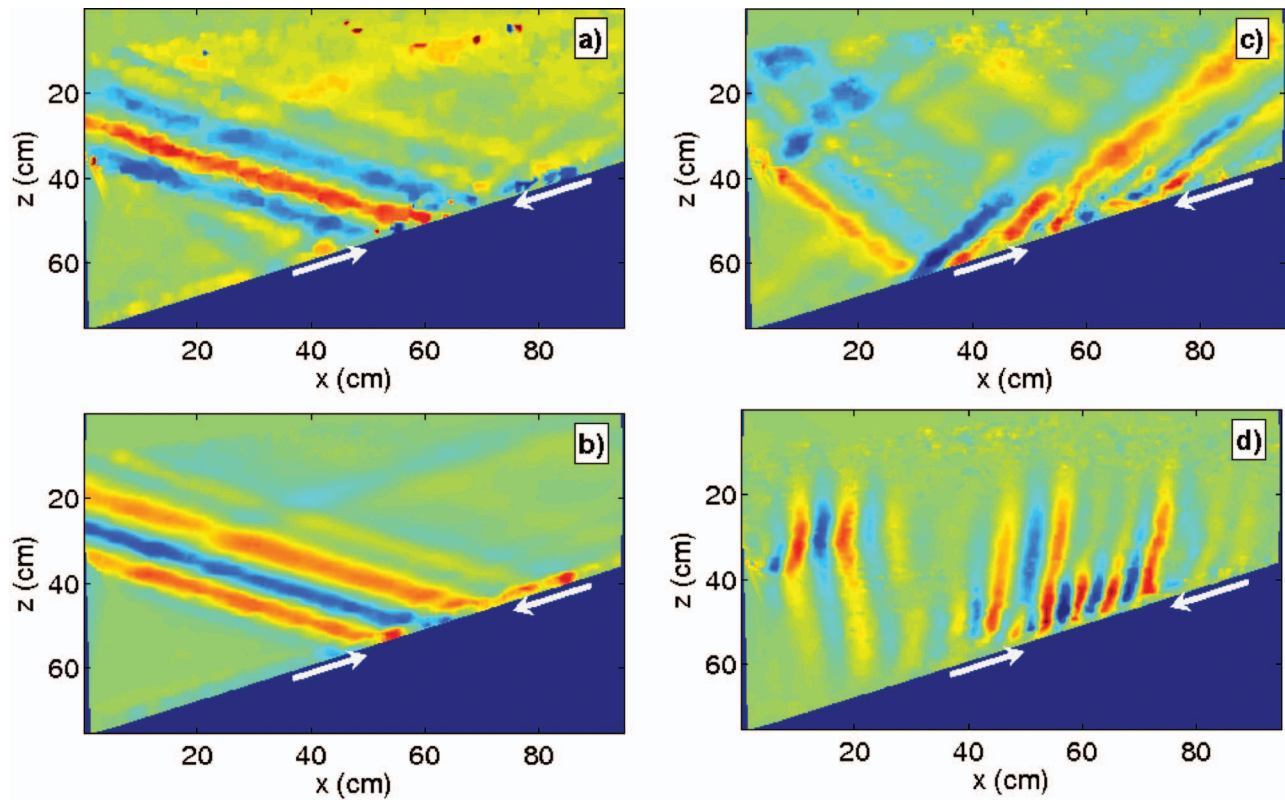
FIG. 5. (Color) False-color velocity pattern in the vertical (x,z) plane for the critical run 4 (see Table I). Panel (a) presents the instantaneous horizontal velocity field $u(x,z,t)$ while panel (b) shows the phase-averaged velocity $\langle u \rangle_1$. Panels (c) and (d) show, respectively, the second $\langle w \rangle_2$ and third $\langle w \rangle_3$ harmonics of the vertical velocity, $\langle w \rangle_n$, in the case of run 4 (see Table I). The two white arrows define the impinging region of the incident beam. In panels (c) and (d), the rays at the left of this region should thus not be taken into account: they have been generated by the screen. The maximum velocity in panels (a) and (b) is 2 mm s^{-1}, and in panels (c) and (d), 0.4 mm s^{-1}.

this is the first case in which the third harmonic has been observed, and even more importantly, this is the first report of experimental quantitative measurements.

It is important to notice that the vertical velocity field is presented in Figs. 5(c) and 5(d), rather than the horizontal one as in the first two panels. Indeed, as the second and third harmonics propagation angles are much steeper, the horizontal velocity field is of lower quality.

An alternative possibility to keep the spatial conformation of the reflection process while distinguishing the different harmonics is to consider the specific kinetic energy density field of each harmonic, which can be deduced from Eq. (4) as

$$\langle E \rangle_n (x,y,\phi) = \tfrac{1}{2}[\langle u \rangle_n^2 + \langle w \rangle_n^2]. \qquad (6)$$

An example is shown in Fig. 6 for the subcritical run 2. One clearly distinguishes the incident beam impinging on the slope, and reflected downslope. It is clear that such energy plots give less contrasted results than the velocity ones as in Fig. 5. They are nevertheless extremely useful for amplitude estimates along cross sections of the beam, as discussed below.

B. Mechanism of wavelength selection

The spectral decomposition presented in the previous section allows precise wavelength measurements across the different beams, even in the impact zone. As the reflection surface is expected to play a key role in wavelength selection via boundary effects, we have focused our study in the boundary region along the slope.

In Fig. 7(a), the contour plots of the filtered first harmonic (incident) and of the third harmonic (emitted) are superimposed in order to show the along-slope wavelength selection. It is clearly visible that the distance between the emitted phase lines has been strongly reduced compared to the incident ones. We emphasize that the wavelength selection mechanism appears to occur along the slope, where the
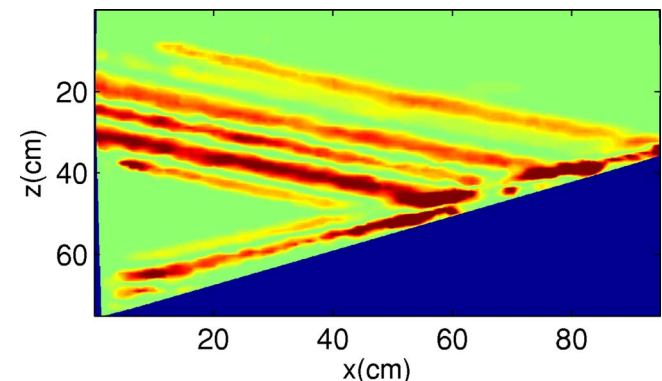

FIG. 6. False-color energy pattern. The specific kinetic energy density of the first harmonic, $\langle E \rangle_1$, is shown in the vertical (x,z) plane for the subcritical run 2 (see Table I). The maximum value is 5×10^{-3} cm^2 s^{-2}.
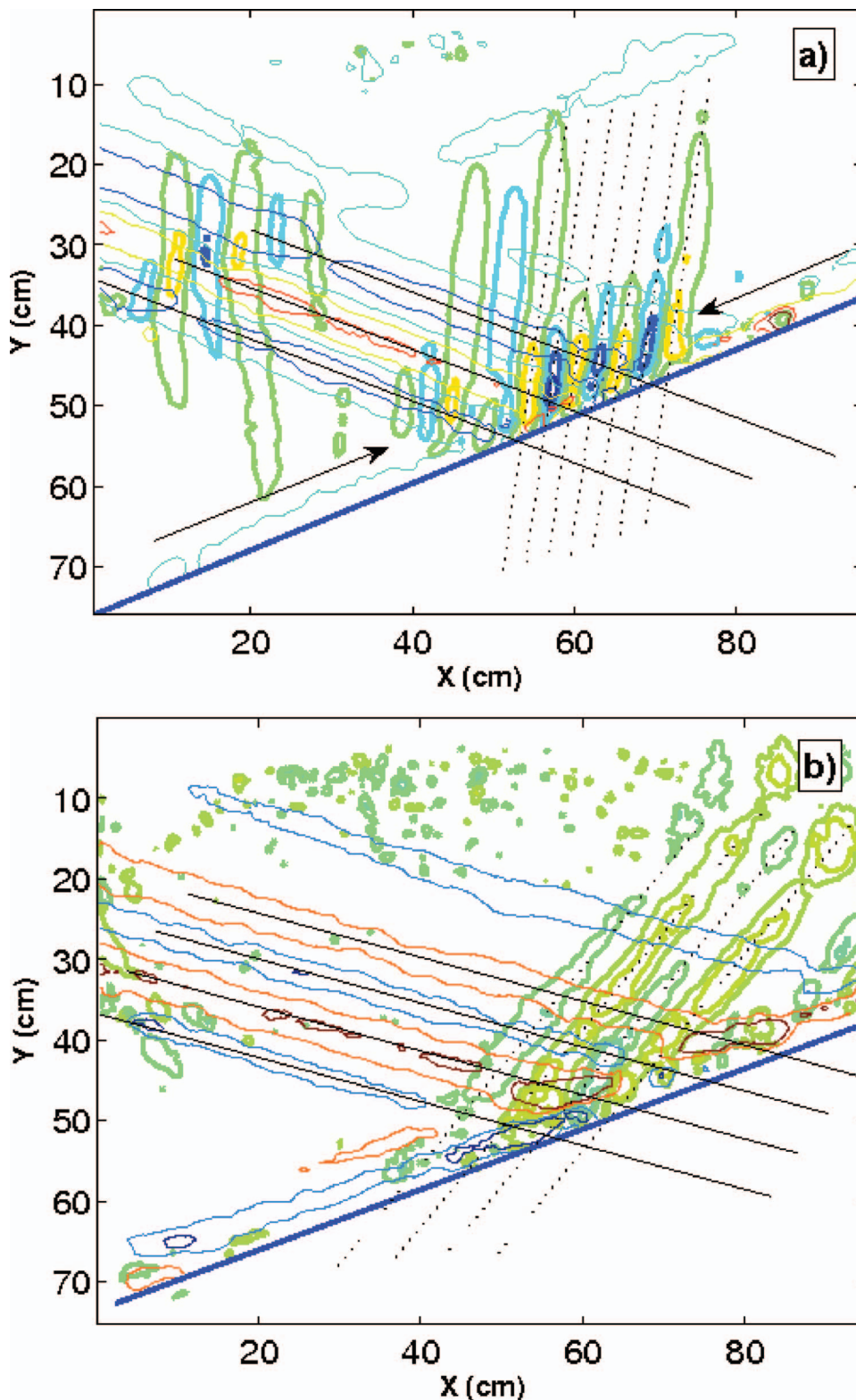
FIG. 7. (Color) Superposition of the vertical velocities contour plots of the incident first harmonic (normal) and of the emitted third harmonic (bold). Panel (a) presents the critical case (run 4) while panel (b) shows the *subcritical* case (run 2). The solid lines show the phase lines of the incident first harmonic $\langle w \rangle_1$ while the dashed ones correspond to the phase lines of the emitted third harmonic $\langle w \rangle_3$. The two arrows in panel (a) indicate precisely the along-slope cross-section used in Fig. 8.

superposition of the incident and the reflected beams generates nonlinear interactions. Assuming that this inner region plays a key role in the reflection of internal waves,[3] the only relevant dynamical behavior of the wave field has to be taken at $z'=0$, where the incident and the emitted waves can both be written as $\psi(z'=0)=A \exp[i(k_{x'}x' - \omega t)]$, the amplitude A being different for the incident and reflected waves. Nonlin-

ear interactions may lead to second or third harmonics terms such as $\psi_2(z'=0)=A_2 \exp[2i(k_{x'}x' - \omega t)]$ or $\psi_3(z'=0)=A \exp[3i(k_{x'}x' - \omega t)]$. The *along-slope* wavelength of the third harmonic is thus reduced by a factor 3, as highlighted in Fig. 7(a) by the phase line intersections with the slope.

To gain further insight, Fig. 8 presents quantitative measurements of this effect in the *supercritical* case 5. The cross-
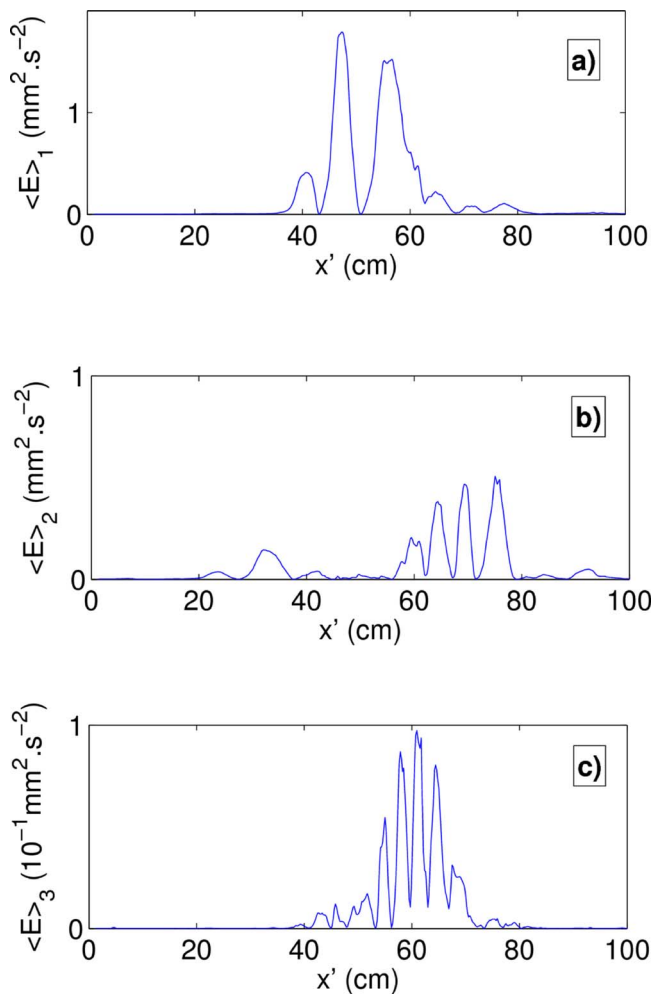
FIG. 8. Along-slope sections of the energy of the incident first harmonic (a), second harmonic (b), and of the emitted third harmonic (c) in the supercritical case (run 5). The sections were obtained at 7 cm from the slope, as indicated by the arrows in Fig. 7(a). Note the difference in units for the ordinates.
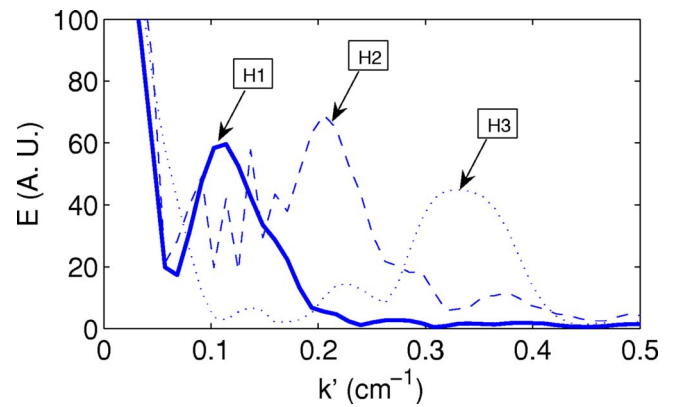

FIG. 9. Spatial Fourier transform of the along-slope sections presented in Fig. 8. The solid line corresponds to $\langle E \rangle_1$ [Fig. 8(a)], the dashed one to $\langle E \rangle_2$ [Fig. 8(b)], and the dotted one to $\langle E \rangle_3$ [Fig. 8(c)]. This picture emphasizes the wave-vector tripling.

sections of the first three harmonics at a fixed distance from the slope are presented. The difference in x' location is of a purely geometrical origin and decreases, of course, when the cross-section is taken closer to the slope. These pictures are analogous to the theoretical results presented by Tabaei, Akylas, and Lamb in Figs. 9(a)–9(d) of Ref. 20.

Let us stress that the above quantitative comparisons are possible despite the large difference between the incident and emitted amplitudes. The automatic elimination of wrong vectors in the measurements by the high-quality cross-correlation PIV algorithm (designed by Fincham and Delerce[5]) is the key point here to achieve this goal. The measurements are indeed sufficiently precise to provide meaningful results even when the relative energy ratio between successive harmonics is approximately 0.1. This last ratio is of course directly linked to the parameter ε, used in Refs. 3 and 20 for the small-amplitude asymptotic expansion to describe theoretically the laboratory reflection process. This is consequently not a limiting factor.

The nonlinear wavelength selection can be clearly highlighted using the above three pictures. Indeed, Fig. 9 presents their spatial Fourier transform and clearly emphasizes that the wavelength of the nth harmonic is $n\lambda$, explaining the wave-vector tripling visible in Fig. 7(a) as theoretically predicted by Tabaei, Akylas, and Lamb.[20]

Experimental results in subcritical cases have unexpectedly revealed an apparent different mechanism for the wavelength selection, when the slope angle α is larger than θ, the angle of energy propagation. A typical example is shown in Fig. 7(b). The second harmonic has disappeared and the wavelength of the third harmonic is equal to the incident wave when it is projected along the slope. This possibility was already mentioned by Thorpe[22] since third-order nonlinear interaction along the slope ($z'=0$) may lead to third harmonics of the form $\psi_3(z'=0)=A \exp[i(k_{x'}x'-3\omega t)]$, where the temporal frequency is tripled while the spatial frequency is kept constant. This is, to our knowledge, the first experimental evidence of this possible nonlinear interaction. The transition from the supercritical (third harmonics along-slope wave-vector tripling and second harmonics along-slope wave-vector doubling) to the subcritical case (third harmonics along-slope wave-vector conservation and absence of second harmonics) is visible in Fig. 7(a), where for the critical case, both wavelengths are present at the frequency 3ω (same along-slope wavelength on the left of the impact zone, tripled on the right). However, this transition remains unexplained.

C. Evanescent harmonics

The angles of propagation of the different harmonics have been measured on the filtered patterns. All the results are listed in Table II for the five runs of Table I. The values are also plotted in Fig. 10 as a function of the pulsation ω and of the harmonic number n. Figure 10(a) attests that the first and second harmonics are in perfect agreement with what is theoretically expected: all corresponding symbols are on the straight line $\omega = N \sin \theta$. This is not the case for the third harmonic in the last three runs. When the sine of the propagation angle is plotted versus the number of the harmonic as in Fig. 10(b), one also sees that the third harmonic is not aligned with the first two for runs 3–5.

TABLE II. Experimentally measured angles of propagation for the three different harmonics. The precision of the measurements is smaller than half a degree. The characteristics of the five runs are given in Table I.

Run	1	2	3	4	5
θ_1 (deg)	12	16.5	19.5	22.5	25
θ_2 (deg)	26	35	41	48	54
θ_3 (deg)	43	52	?65	85	81.5
$\sin \theta_1$	0.21	0.28	0.33	0.38	0.42
$\sin \theta_2$	0.44	0.57	0.66	0.74	0.81
$\sin \theta_3$	0.68	0.79	0.91	1.00	0.99

FIG. 11. (Color online) False-color velocity pattern. The vertical third harmonic $\langle w \rangle_3$ is shown in the (x, z) plane for run 5. The maximum velocity is 0.4 mm s^{-1}.

As discussed, for example, by Tabaei *et al.*,[20] the maximum incident angle θ for which the nth harmonic can propagate is $\sin^{-1}(1/n)$. For larger angles, the corresponding harmonic will be evanescent since the frequency would be larger than the Brunt-Väisälä top band frequency. For $\theta > \sin^{-1}(1/3) \simeq 19°$, the third harmonic is thus found to be evanescent: this is the case for runs 3–5 of Table II, explaining the three symbols not on the line in Fig. 10(a). In these cases, the third harmonic generated in the impact zone cannot propagate, and is thus trapped along the slope. This is what is shown in Fig. 11. Evanescent modes were also found experimentally[21] in a different context, namely nonlinear nonresonant interaction between two internal wave rays.

If the evanescence of the wave is clarified, an angle of propagation, *not vertical*, can be measured as shown for run 5 in Fig. 11. Another case is also visible in Fig. 5(d). It is possible to theoretically explain this angle as follows.
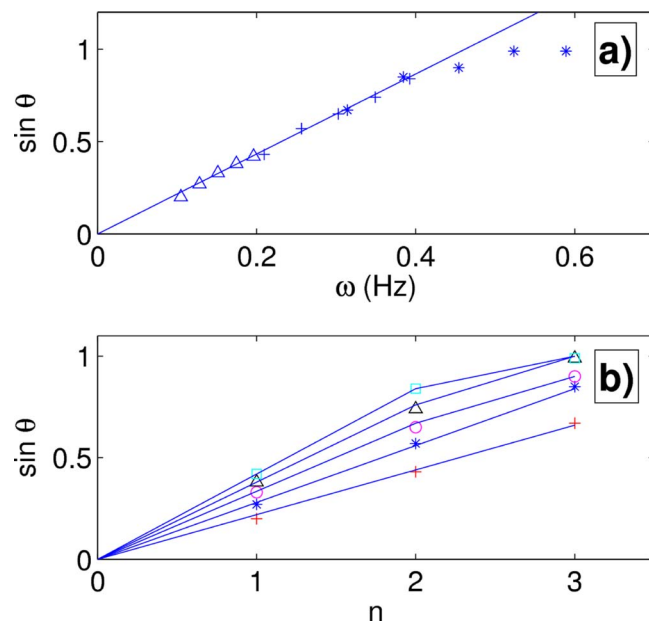
Considering the linear equation (3) valid for internal waves within the Boussinesq approximation, let us look for stream-function solutions ψ, evanescent in the z' direction, i.e., orthogonally to the slope, but propagating in the x and z direction (see Fig. 3 for the definitions of these variables). Introducing the two components of the wave vector (k_x, k_z) and δ, the attenuation (or evanescence) length, we thus look for solutions as

$$\psi(x, z, t) = \psi_0 e^{i(k_x x + k_z z - \omega t)} e^{-z'/\delta} \tag{7}$$

$$= \psi_0 e^{(i k_x + \sin \alpha / \delta) x + (i k_z - \cos \alpha / \delta) z - i \omega t}, \tag{8}$$

since $z' = z \cos \alpha - x \sin \alpha$. Introducing the above ansatz in Eq. (3) leads to a complex equation. Separating real and imaginary parts and defining $\gamma = \omega/N$, we get

$$\delta^2 = \frac{\cos^2 \alpha}{k_x^2} \frac{\gamma^2 - \sin^2 \alpha}{\gamma^2 - 1}, \tag{9}$$

$$k_z = k_x \tan \alpha (1 - \gamma^{-2}). \tag{10}$$

For $\gamma > 1$, we can thus define the angle of propagation of the evanescent wave $\theta_{ev} = \text{atan}(k_x/k_z)$. Equation (10) leads to

$$\theta_{ev}(\alpha, \gamma) = \text{atan}\left(\frac{\cot \alpha}{1 - \gamma^{-2}}\right). \tag{11}$$

Figure 12 attests that the experimental results agree very well with formula (11) for runs 4 and 5. Unexpectedly, the case

FIG. 10. Angular dispersion for the different harmonics. Panel (a) presents the sine of the different angles of propagations vs the wave frequency ω. The different symbols corresponds to the first (triangles), second (plus), and third harmonic (stars). The solid line corresponds to the theoretical law $\omega = N \sin \theta$ for $2\pi N^{-1} = 13.6$ s. Panel (b) presents the same data as a function of the number of the harmonics for runs 1–5 (plus, stars, circles, dots, and squares, respectively). Error bars are smaller than the symbol size.
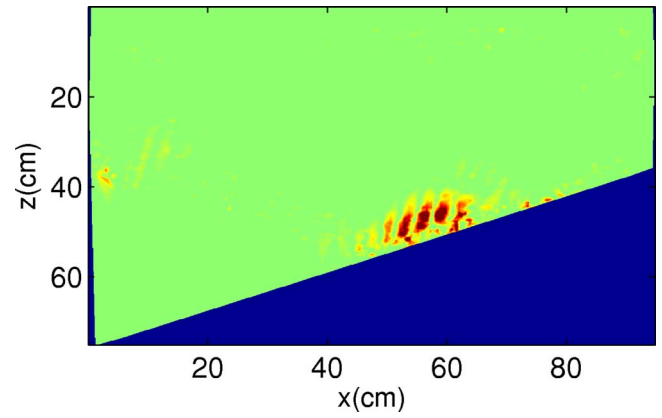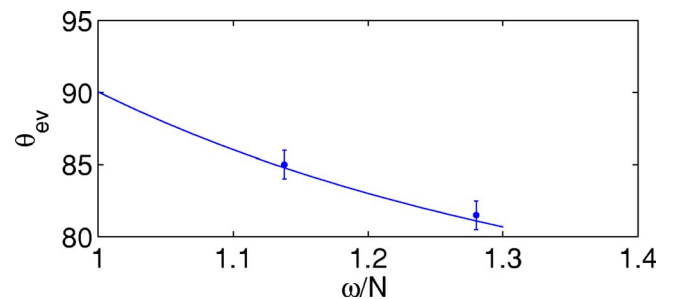

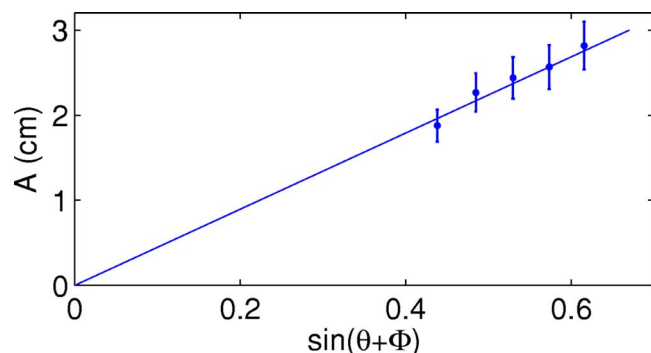FIG. 12. Angle of propagation of the evanescent third harmonic for runs 4 and 5.

FIG. 13. Experimental measure of the displacement amplitude of the emitted wave as a function of the emission angle θ for the five runs of Table I.

FIG. 14. Velocity amplitudes of the first three harmonics as functions of the difference between the emission angle θ and the slope angle α for the five runs of Table I. Stars, triangles, and crosses correspond to the first, second, and third harmonics, respectively.

$\theta = 19°$, for which the third harmonic is at the limit of evanescence, is, however, not described by the above model. Note also that an alternative theoretical description is proposed in Ref. 20.

D. Amplitude measurements

The determination of wave amplitudes is complicated by the beam-like appearance of the displacement field. Indeed, local temporal spectral analysis is not sufficient to provide reliable energy measurements, as phase and group speed are orthogonal. Spatial integration across the beam are needed to accurately evaluate the amount of energy involved in each harmonics.

First, to validate the method of measurement, the mean displacement amplitude $A = \sqrt{u^2 + w^2}/\omega$ of the incident beam is plotted as a function of the incidence angle. The wave maker being tilted at a constant angle $\Phi = 13°$ with the horizontal, it induces a shear motion perpendicular to itself (see Fig. 3). The propagating part of this motion is thus expected to be proportional to $\sin(\theta + \Phi)$. The very good agreement shown in Fig. 13 justifies *a posteriori* the method.

Determining the importance of the different harmonics emitted after the reflection process is an important issue to understand and hence describe theoretically the reflection process. After exploring several possibilities, it appears that the best method to quantitatively characterize the measurements is the following one. First, it is important to distinguish the two components of velocity vectors, parallel to the slope and orthogonal to it. The second one vanishes clearly close to the slope, thus satisfying the expected boundary conditions. Away from the slope, because of the possibilities of evanescence it is very delicate to get reliable amplitudes. On the contrary, the along-slope component of the velocities is easier to deal with. It has no reason to vanish close to the slope and definitely did not. We have thus measured the amplitude of the wave by determining the maximum value of the different harmonics. Results are collected and shown in Fig. 14. The velocity amplitudes for the second and third harmonics are four times smaller than for the first harmonic, even for runs 4 and 5 when the third harmonic is evanescent. It is important to emphasize that the difference between the second and third harmonics is small.
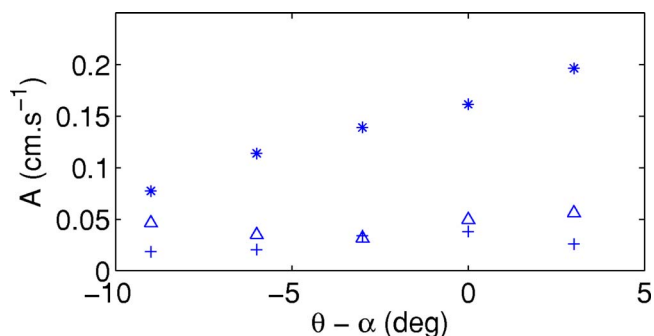
IV. CONCLUSION

In this paper, we have reported *quantitative* laboratory measurements of the propagation of internal waves. Our experimental setup produces an incident beam of high quality. Its large scale allows us to reach large Reynolds numbers, such that the effects of dissipation on the propagation are negligible. This is no longer true for the critical reflection mechanism, which involves a strong reduction of the wavelength, hence increased viscous effects. Thus, one obtains a steady regime compatible with the hypothesis of previous theoretical models.[3,20]

The wave vector of the frequency nth harmonics, projected along the slope, is found to be proportional to n in the supercritical case. This is in agreement with the theory.[20] A different selection mechanism is, however, observed in the subcritical case, for which the wave number is equal to the incident one. This is in contradiction with Ref. 20 but in agreement with a more simple analysis previously proposed by Thorpe.[22]

Harmonics with frequency higher than N cannot propagate and remain trapped near the slope. We document their existence and explain their spatial structure.

The long two-dimensional internal wave exciter produces very weak transversal y variations, apparently justifying two-dimensional predictions in the (x, z) plane. Considering a rotating tank would require us to address the much tougher, fully three-dimensional equation, and it is not *a priori* clear what will happen. Work along these lines is in progress.

ACKNOWLEDGMENTS

[1] D. Cacchione and C. Wunsch, "Experimental study of internal waves over a slope," J. Fluid Mech. **66**, 223 (1974).
[2] T. Dauxois, A. Didier, and E. Falcon, "Observation of near-critical reflection of internal waves in a stably stratified fluid," Phys. Fluids **16**, 1936 (2004).
[3] T. Dauxois and W. R. Young, "Near-critical reflection of internal waves,"

J. Fluid Mech. **390**, 271 (1999).

[4]C. C. Eriksen, "Implications of ocean bottom reflection for internal wave spectra and mixing," J. Phys. Oceanogr. **15**, 1145 (1985).

[5]A. Fincham and G. Delerce, "Advanced optimization of correlation imaging velocimetry algorithms," Exp. Fluids **29**, 13 (2000).

[6]G. N. Ivey and R. I. Nokes, "Vertical mixing due to the breaking of critical internal waves on sloping boundaries," J. Fluid Mech. **204**, 479 (1989).

[7]G. N. Ivey, K. B. Winters, and I. P. D. De Silva, "Turbulent mixing in a sloping benthic boundary layer energized by internal waves," J. Fluid Mech. **418**, 59 (2000).

[8]A. Javam, J. Imberger, and S. W. Armfield, "Numerical study of internal wave reflection from sloping boundaries," J. Fluid Mech. **396**, 183 (1999).

[9]A. Javam, J. Imberger, and S. W. Armfield, "Numerical study of internal wave-wave interactions in a stratified fluid," J. Fluid Mech. **415**, 65 (2000).

[10]L. R. M. Maas, "Wave focusing and ensuing mean flow due to symmetry breaking in rotating fluids," J. Fluid Mech. **437**, 13 (2001).

[11]L. R. M. Maas, D. Benielli, J. Sommeria, and F.-P. A. Lam, "Observation of an internal wave attractor in a confined stably stratified fluid," Nature (London) **388**, 557 (1997).

[12]L. R. M. Maas and F.-P. A. Lam, "Geometric focusing of internal waves," J. Fluid Mech. **300**, 1 (1995).

[13]E. E. McPhee-Shaw and E. Kunze, "Boundary layer intrusions from a sloping bottom: A mechanism for generating intermediate nepheloid layers," J. Geophys. Res. **107**, 31 (2002).

[14]D. E. Mowbray and B. S. H. Rarity, "A theoretical and experimental investigation of the phase configuration of internal waves of small amplitude in a density-stratified liquid," J. Fluid Mech. **28**, 1 (1967).

[15]A. Fincham, O. Praud, and J. Sommeria, "Decaying grid turbulence in a strongly stratified fluid," J. Fluid Mech. **522**, 1 (2005).

[16]T. Peacock and A. Tabei, "Visualization of nonlinear effects in reflecting internal wave beams," Phys. Fluids **17**, 061702 (2005).

[17]O. M. Philipps, *The Dynamics of the Upper Ocean* (Cambridge University Press, London, 1977).

[18]D. N. Slinn and J. J. Riley, "Turbulent dynamics of a critically reflecting internal gravity wave," Theor. Comput. Fluid Dyn. **11**, 281 (1998).

[19]B. R. Sutherland, "Propagation and reflection of internal waves," Phys. Fluids **11**, 1081 (1999).

[20]A. Tabaei, T. R. Akylas, and K. Lamb, "Nonlinear effects in reflecting and colliding internal wave beams," J. Fluid Mech. **526**, 217 (2005).

[21]S. G. Teoh, G. N. Ivey, and J. Imberger, "Laboratory study of the interaction between two internal wave rays," J. Fluid Mech. **336**, 91 (1997).

[22]S. A. Thorpe, "On the reflection of a strain of finite-amplitude internal waves from a uniform slope," J. Fluid Mech. **178**, 279 (1987).

[23]S. A. Thorpe and A. P. Haines, "A note on observations of wave reflection on a 20 degree slope," J. Fluid Mech. **178**, 279 (1987) (appendix to Ref. 22).

[24]O. Zikanov and D. Slinn, "Along-slope current generation by obliquely incident internal waves," J. Fluid Mech. **445**, 235 (2001).